View metadata, citation and similar papers at core.ac.uk

brought to you by CORE

provided by Woods Hole Open Access Se

JOURNAL OF GEOPHYSICAL RESEARCH, VOL. 112, B01205, doi:10.1029/2006JB004301, 2007

Click Here for Full Article

Olivine friction at the base of oceanic seismogenic zones

Margaret S. Boettcher,[1,2] Greg Hirth,[1] and Brian Evans[3]

Received 19 January 2006; revised 5 September 2006; accepted 28 September 2006; published 31 January 2007.

[1] We investigate the strength and frictional behavior of olivine aggregates at temperatures and effective confining pressures similar to those at the base of the seismogenic zone on a typical ridge transform fault. Triaxial compression tests were conducted on dry olivine powder (grain size $\leq$60 μm) at effective confining pressures between 50 and 300 MPa (using Argon as a pore fluid), temperatures between 600°C and 1000°C, and axial displacement rates from 0.06 to 60 μm/s (axial strain rates from 3×10^{-6} to 3×10^{-3} s^{-1}). Yielding shows a negative pressure dependence, consistent with predictions for shear enhanced compaction and with the observation that samples exhibit compaction during the initial stages of the experiments. A combination of mechanical data and microstructural observations demonstrate that deformation was accommodated by frictional processes. Sample strengths were pressure-dependent and nearly independent of temperature. Localized shear zones formed in initially homogeneous aggregates early in the experiments. The frictional response to changes in loading rate is well described by rate and state constitutive laws, with a transition from velocity-weakening to velocity-strengthening at 1000°C. Microstructural observations and physical models indicate that plastic yielding of asperities at high temperatures and low axial strain rates stabilizes frictional sliding. Extrapolation of our experimental data to geologic strain rates indicates that a transition from velocity weakening to velocity strengthening occurs at approximately 600°C, consistent with the focal depths of earthquakes in the oceanic lithosphere.

Citation: Boettcher, M. S., G. Hirth, and B. Evans (2007), Olivine friction at the base of oceanic seismogenic zones, *J. Geophys. Res.*, *112*, B01205, doi:10.1029/2006JB004301.

1. Introduction

[2] While the composition of the oceanic lithosphere is probably the simplest and most well constrained of any seismogenic region on Earth, few data on its frictional properties exist. Comparison of the depths of oceanic earthquakes with thermal models indicates that the seismicity is thermally bounded [*Wiens and Stein*, 1983; *Engeln et al.*, 1986; *Bergman and Solomon*, 1988; *Stein and Pelayo*, 1991; *Scholz*, 2002]. The most recent studies of mantle seismicity [*Wilcock et al.*, 1990; *Abercrombie and Ekström*, 2003] and thermal models [*McKenzie et al.*, 2005] suggest that seismicity is restricted to depths where the temperature is less than approximately 600°C, indicating that a transition from unstable to stable frictional sliding occurs with an increase in temperature above 600°C. By contrast, previous experimental work on the frictional behavior of olivine aggregates showed this stability transition at significantly lower temperatures, $T \approx 200$°C [*Stesky et al.*, 1974; *Stesky*, 1978a, 1978b]. We present new experimental data that are consistent with the geophysical observations.

[3] In our experiments we observe shear localization in olivine aggregates and investigate the experimental conditions at which localized sliding transitions from exhibiting velocity weakening to velocity strengthening behavior. We use microstructures to constrain deformation mechanisms at grain-to-grain contacts and discuss the processes controlling the transition from unstable to stable deformation in the context of rate and state friction. Finally, we extrapolate our laboratory results to geologic conditions using flow laws for low-temperature plasticity of olivine [*Goetze*, 1978; *Evans and Goetze*, 1979].

2. Experimental Design

[4] Deformation experiments were conducted in a servo-controlled, internally heated, gas-medium apparatus from "Paterson Instruments" [see *Paterson*, 1990; *Xiao and Evans*, 2003]. Crystals of San Carlos olivine ($\sim Fo_{91}$) were ground to a powder, producing a starting grain size of less than 60 μm. The powders were oven dried, then cold pressed at approximately 5 MPa into 26 mm long copper jackets with inner and outer diameters of 10 mm and 11.2 mm,

[1]Marine Geology and Geophysics, Woods Hole Oceanographic Institution, Woods Hole, Massachusetts, USA.
[2]Now at United States Geological Survey, Menlo Park, California, USA.
[3]Earth, Atmospheric, and Planetary Sciences, Massachusetts Institute of Technology, Cambridge, Massachusetts, USA.

Copyright 2007 by the American Geophysical Union.
0148-0227/07/2006JB004301$09.00

Table 1. Experimental Parameters

Experiment	T, °C	P_C^{eff}, MPa	P_C, MPa	V, μm/s	σ_{max},[a] MPa	d_{max}, mm	axial ϵ, %	(a-b), −/+
OF-01	740	300	300	0.6	395	2.37	10.4	–
OF-02	800	300	300	0.6	510	4.22	20.8	–
OF-03[b]	800	300	300	n/a	n/a	n/a	0	n/a
OF-04	800	300	310	0.6	495	4.56	21.4	–
OF-05[c]	800	50	300	0.6, 6	125	2.66	14.1	–
OF-06[c]	800	200	310	0.6, 6	370	3.39	16.1	–
OF-07[d]	1000	200	300	0.6, 6	380	5.18	24.1	–,+
OF-08[b,d]	1000	200	300	0.6	259	1.22	6.2	n/a
OF-11[b,d]	1000	200	300	0.6	174	1.11	4.9	n/a
OF-12[b,d,e]	1000	200	300	0.6	187	0.97	4.9	n/a
OF-13[b,d,f]	800	100	300	0.06 – 60	205	4.80	23.8	–
OF-15[d,f]	1000	100	300	0.06 – 60	225	4.11	22.6	–,+
OF-19[f]	600	100	125	0.06 – 60	215	3.83	20.9	–

[a]Maximum differential stress reached while subject to a loading rate of 0.6 μm/s.
[b]Experiment was stopped after little to no axial strain.
[c]Volumetric strain was recorded and a correction for a leak was applied to the raw data.
[d]Volumetric strain was recorded.
[e]Samples were oxidized to decorate dislocations.
[f]Enstatite strain markers were included in the sample volume.

respectively. In a few experiments, two thin layers of enstatite powder were inserted during cold pressing to serve as strain markers. Experiments were conducted at temperatures of 600°C $\leq$ T $\leq$ 1000°C and effective confining pressures of 50 MPa $\leq P_C^{eff} \leq$ 300 MPa, where P_C^{eff} is confining pressure minus pore pressure $P_C^{eff} = P_C - P_P$. To reach the desired P_C^{eff} and T, confining pressure and pore pressure were increased simultaneously, followed by heating at 0.25°C/s. Argon was used for both the confining and pore fluid media; volumetric strain was measured with a volumometer. In some cases a small pore pressure leak occurred through the volumometer. For these samples, noted in Table 1, the leak rate prior to deformation was measured. We assumed that the leak rate remained constant throughout the experiment and corrected the raw volumetric strain data accordingly.

[5] Prior to deformation, each sample was subjected to an hour-long hot press at the experimental pressure and temperature conditions. A micrograph of a sample that was removed after the hot-pressing step is shown in Figure 1. After hot-pressing, we confirmed that samples were permeable by applying a fluid pressure wave to the upstream end of the sample and observing the wave with little to no delay on the downstream side. Experiments were conducted at axial displacement rates of 0.06 μm/s $\leq V \leq$ 60 μm/s, resulting in bulk axial strain rates of 3×10^{-6} s^{-1} $\leq \dot{\epsilon} \leq 3 \times 10^{-3}$ s^{-1}. All experiments were terminated prior to 5.5 mm of axial displacement. This constraint limited rotations of the stress field caused by buckling of the load column and ensured that the jacket separating the pore fluid from the confining pressure did not rupture. An example of a deformed specimen illustrating the sample assembly is shown in Figure 2.

[6] After deformation, samples were impregnated with epoxy, cut perpendicular to the shear zone, and thin sections were prepared to observe microstructures. Some deformed samples were heated in air for 1 hour at 900°C to decorate dislocations [*Kohlstedt et al.*, 1976] prior to thin section preparation. Raw data in the form of load, axial displacement, and volumometer displacement were converted to differential stress, axial strain, and volumetric strain, assuming homogeneous deformation. For samples with no pore fluid pressure, differential stress was calculated assuming a constant sample volume. When volume changes were recorded, they were used to obtain differential stress, which reduced the calculated values by 0.5–3%.

3. Results

[7] The results of 13 triaxial deformation tests are summarized in Table 1. As illustrated in Figure 3, differential stress versus displacement behavior was reproducible, showing only modest variation throughout the experiment for tests conducted at the same conditions (e.g., OF-02 and OF-04 in Table 1).

3.1. Mechanical Data

[8] Differential stress versus axial displacement curves for samples deformed at 800°C show that maximum sample strength increases with increasing effective confining pressure (Figure 3). In each experiment the initial stages

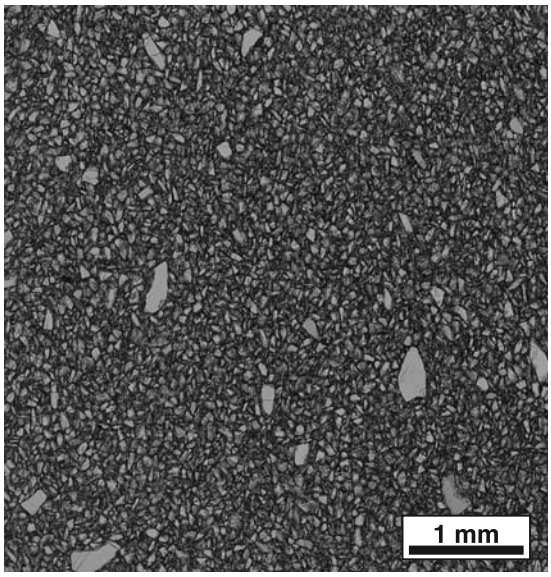

Figure 1. Optical micrograph (plane light) of sample OF-03 hot-pressed for 1 hour at 800°C and P_C^{eff} = 300 MPa.

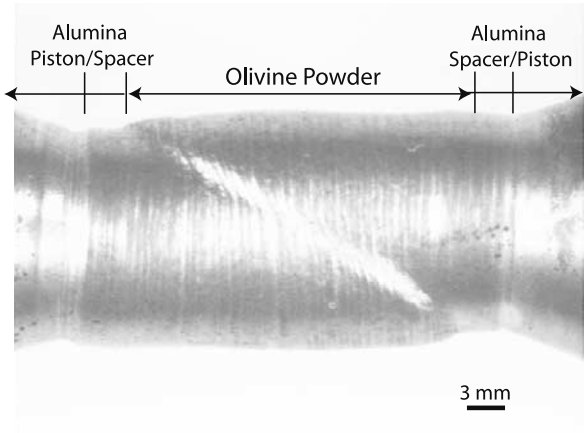

Figure 2. An initially cylindrical olivine aggregate was deformed at P_C^{eff} = 50 MPa, T = 800°C, resulting in a localized shear zone oriented approximately 30 degrees to the shortening direction (horizontal in photograph). Sample assembly includes alumina (Al_2O_3) pistons, 3 mm thick alumina spacers, and the sample of olivine powder. The assembly is enclosed within a copper jacket.

of deformation were nominally elastic and were followed by an interval of strain-hardening. Increasing effective confining pressure resulted in lower yield strength and the continuation of strain hardening to greater axial displacements. At P_C^{eff} = 200 and 300 MPa strain-hardening gave way to stick-slip instabilities after about 3 mm of axial displacement. At P_C^{eff} = 50 and 100 MPa the samples reached a steady-state frictional sliding stress at 1.7–2.7 mm of axial displacement, after undergoing a 10–15% decrease in strength.

[9] The maximum sample strength showed little temperature dependence (Figure 4). After about 2.5 mm of axial displacement the stress-displacement curves shown in Figure 4 all approach a differential stress of $\sigma_1 - \sigma_3 \approx$ 200 MPa, where σ_1 and σ_3 are the maximum and minimum compressive stresses. However, temperature did affect the onset of yielding and the rate of hardening. At higher temperatures, yielding occurred at lower stress and the hardening rate decreased for a given P_C^{eff}. Thus greater axial displacements were required for samples to achieve their peak differential stress during higher temperature tests.

[10] The pressure dependence of maximum strength is illustrated with a Mohr diagram in Figure 5. The Mohr circles are drawn using the maximum differential stress measured at V = 0.6 μm/s in each experiment with $\sigma_3 = P_C^{eff}$ (Table 1). A linear fit between $\sigma_1 - \sigma_3$ and P_C^{eff} gives a slope μ' = 1.5 with a y-intercept, which represents the uniaxial compressive strength, of σ_0 = 65 MPa (Figure 5a). The coefficient of friction μ and cohesive strength τ_0 are constrained by the equivalence relations [*Paterson*, 1978],

$$\mu = \frac{\mu'}{2\sqrt{1+\mu'}} \quad (1)$$

and

$$\tau_0 = \frac{\sigma_0}{2\sqrt{1+\mu'}}. \quad (2)$$

Using the linear fit to the differential stress and effective confining pressure data shown in Figure 5a, the data shown in Figure 5b are best fit by μ = 0.5 and τ_0 = 21 MPa. For comparison with standard frictional sliding tests, by assuming negligible cohesive strength at P_C^{eff} = 0 our data predict a decrease in coefficient of friction with increasing effective confining pressure, from μ = 0.7 at P_C^{eff} = 50 MPa to μ = 0.5 at P_C^{eff} = 300 MPa. This decrease in μ with increasing normal stress is consistent with numerous previous results [e.g., *Brace et al.*, 1966; *Byerlee*, 1978; *Shimada et al.*, 1983; *Evans et al.*, 1990; *Escartin et al.*, 1997]. Indeed, if the coefficient of friction were pressure-dependent, then the increase suggested by our data is similar to that predicted by Byerlee's Rule, although the values of μ are somewhat lower. The differential stress measured during our experiments may be underestimated owing to slight bending of the load column and to decreases in the load bearing area as localized sliding progresses.

3.2. Microstructural Observations

[11] Microstructural observations show that deformation localized onto multiple shear zones within the initially homogeneous olivine aggregates. The shear zones are oriented between 30 and 40 degrees to σ_1 and increase in thickness with increasing P_C^{eff} and T. By conducting experiments at a range of conditions we obtained fabrics at various stages of strain localization. In addition, with enstatite strain markers, we were able to quantify the shear displacement along individual shear planes and relate it to the stress-axial displacement history of the sample.

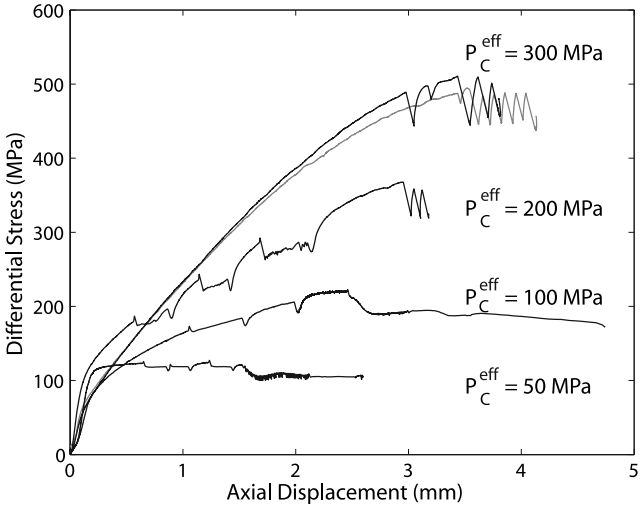

Figure 3. Differential stress versus axial displacement curves for experiments conducted at T = 800°C. The initial loading rate for all experiments was V = 0.6 μm/s. Order-of-magnitude velocity steps were performed between 0.6 and 6.0 μm/s in P_C^{eff} = 50 and 200 MPa experiments and between 0.06 and 60 μm/s in the P_C^{eff} = 100 MPa experiment. Note the similarity in the strength profiles for experiments conducted at P_C^{eff} = 300 MPa.

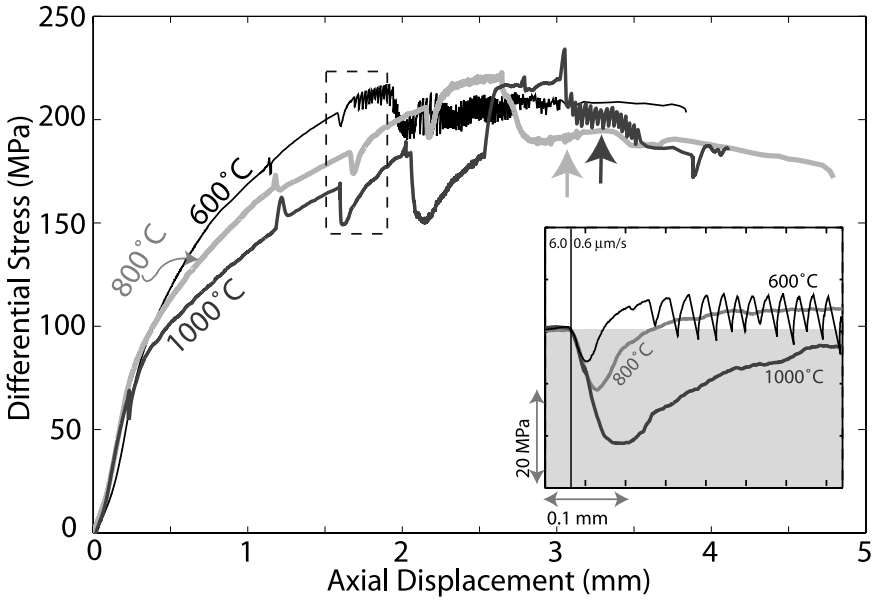

Figure 4. Temperature effect on the strength and frictional behavior of samples deformed at P_C^{eff} = 100 MPa with axial displacement rates of $0.06 \leq V \leq 60$ μm/s. Arrows indicate where localized sliding initiated based on measurement of offsets in enstatite layers. The dashed box indicates the data plotted in the inset, for which the strain-hardening trend was removed and the curves were translated to the same initial strength and the same axial displacement for the velocity step from 6.0 to 0.6 μm/s. The 1000°C data show velocity strengthening (gray field), while velocity weakening (white field) is observed at 600°C and 800°C.

[12] The micrograph shown in Figure 6a illustrates the initial stages of localization in a sample deformed to an axial strain of 10% at 740°C and P_C^{eff} = 300 MPa. A thin band of reduced grain size marks the shear zone. The density of microcracks within large grains is significantly greater than that observed in the sample that was removed after the hot-pressing stage (Figure 1). A well developed, 0.2–1.0 mm thick, shear zone is exhibited in a sample deformed to 16% axial strain at 800°C and P_C^{eff} = 200 MPa (Figure 6b). This sample strain-hardened for nearly 90% of the experiment, followed by three stick-slip instabilities that occurred shortly before the experiment was terminated (Figure 3). The micrographs shown in Figures 6c and 6d, from samples deformed at 800°C and P_C^{eff} = 50 MPa and 1000°C and P_C^{eff} = 200 MPa, respectively, display highly localized, fine-grained shear zones. Figure 6c shows a primary shear plane along with a number of secondary shear planes, indicating that a single slip surface does not

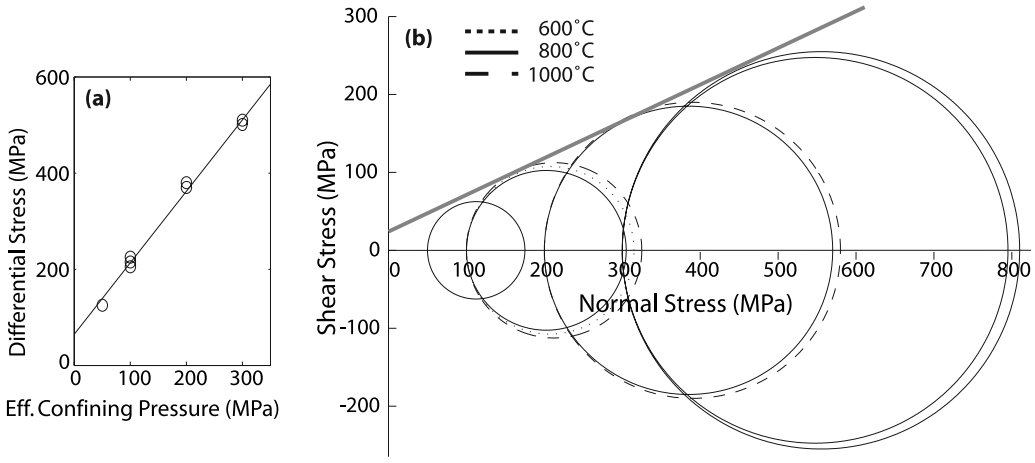

Figure 5. Maximum differential stress increases with effective confining pressure. (a) Linear least squares fit to effective confining pressure versus maximum observed differential stress at V = 0.6 μm/s. (b) Mohr circles, constructed with the data in Figure 5a. Data are shown for tests with maximum axial displacement greater than 3 mm (Table 1). The line approximately tangent to the Mohr circles indicates a coefficient of friction of μ = 0.5.

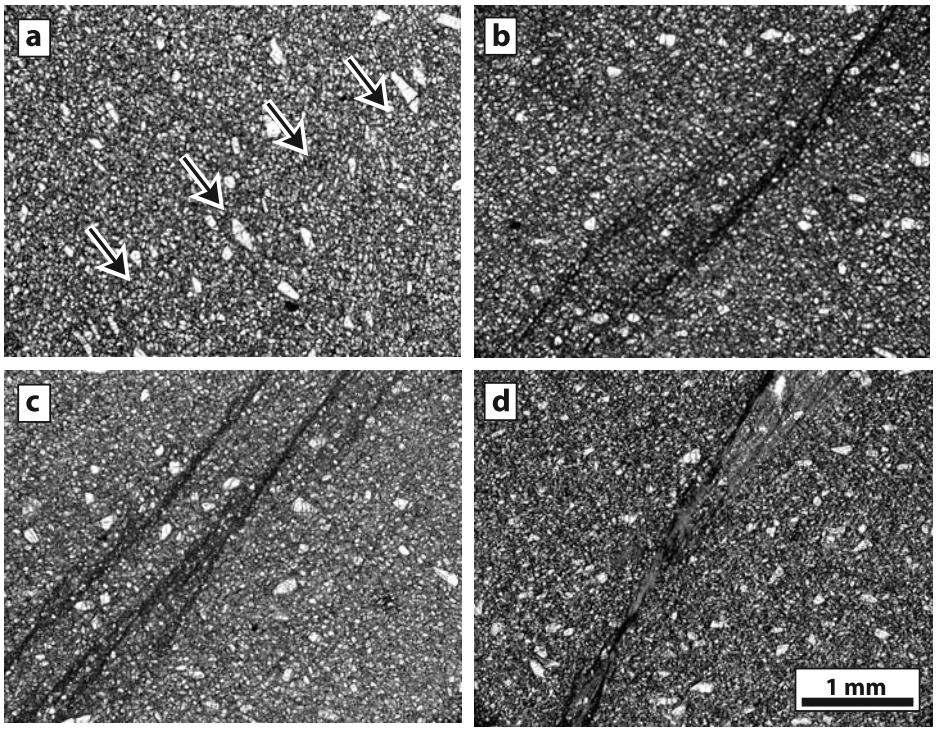

Figure 6. Photomicrographs showing different stages of strain localization in samples deformed under the following conditions: (a) 740°C, P_C^{eff} = 300 MPa, axial ϵ = 10% (OF-01); (b) 800°C, P_C^{eff} = 200 MPa, axial ϵ = 16.1% (OF-06); (c) 800°C, P_C^{eff} = 50 MPa, axial ϵ = 14.1% (OF-05); and (d) 1000°C, P_C^{eff} = 200 MPa, axial ϵ = 24.1% (OF-07). The shortening direction is vertical in all micrographs. The scale shown in Figure 6d applies to all micrographs. Arrows drawn on Figure 6a point to a thin, localized region of reduced grain size.

persist throughout deformation. Similar observations are presented by *Beeler et al.* [1996] for much higher displacement tests on granitic samples. Their experiments showed evidence for migration of the primary shear surface as the run progressed. Our microstructural observations indicate that increased strain and lower pressures promote localization.

[13] The inclusion of enstatite strain markers allowed us to constrain displacements accommodated by the discrete shear zones. Prior to deformation, the layer of enstatite was continuous and nearly perpendicular to the cylindrical axis. In the example shown in Figure 7 for sample OF-13, we measured a total of ~1.9 mm of localized shear displacement; 1.1 mm in the section of shear zone shown in Figure 7 and an additional 0.8 mm on separate shear surfaces. Similar measurements gave 1.6 mm of localized shear displacement for sample OF-15. On the basis of microstructural observations described above, we assume that deformation was fully localized on these discrete shear planes at the end of the experiments. By subtracting the measured shear offsets in the enstatite layers, projected on the sample's cylindrical axis, from the total axial displacements, we obtained the approximate displacement at which the fully localized sliding initiated. The arrows shown in Figure 4 indicate that shear displacement localized soon after the prominent stress drops near the end of the experiments.

[14] Microstructural observations of decorated samples show evidence for crystal-plastic deformation resulting from stress concentrations at grain-to-grain contacts. An example of dislocation microstructures within the San Carlos olivine starting material is shown in Figure 8a. These grains exhibit a low-density of relatively long and curved

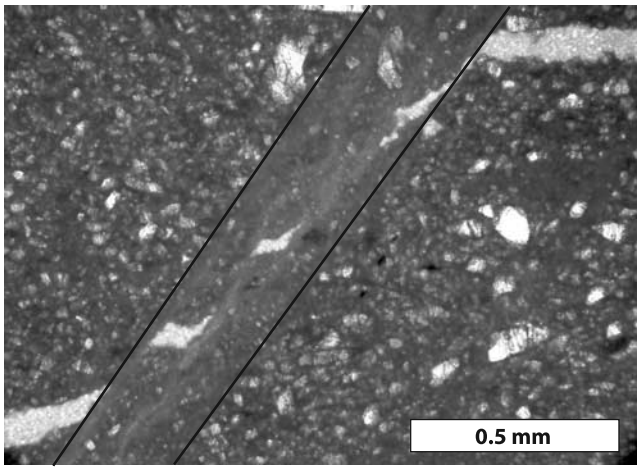

Figure 7. Photomicrograph showing offsets in an enstatite layer (light gray) within an olivine aggregate. The sample was deformed at 800°C and P_C^{eff} = 100 MPa (OF-13); several localized shear planes formed within the fine-grained shear zone, which is denoted by solid black lines. From left to right the four most prominent shear offsets measure 0.22 mm, 0.26 mm, 0.38 mm, and 0.20 mm, respectively.

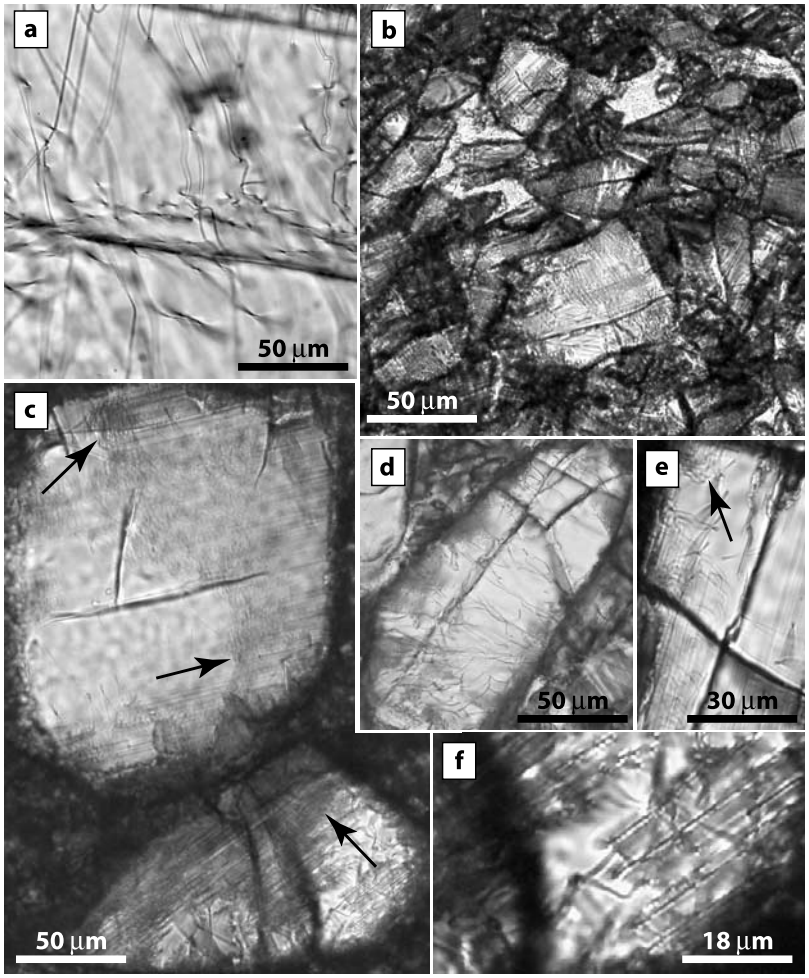

Figure 8. Photomicrographs of decorated dislocations in (a) a single crystal of San Carlos olivine and (b)–(f) grains in a sample deformed at $T = 800°C$ and $P_C^{eff} = 100$ MPa (OF-13). Shortening direction is oriented vertically. Note that the density of dislocations in the deformed grains increases toward grain boundaries with many tangles of dislocations (denoted with black arrows).

dislocations. Subgrain boundaries are also present. By contrast, the dislocation densities in our deformed samples are much higher. As shown in Figure 7, the microstructure away from the shear zones is characterized by relatively large grains within a finer-grained matrix. After decoration, the microstructure in the finer-grained regions is dominated by the oxidized grain boundaries and microcracks, however high and heterogeneous densities of dislocations are visible within grains (Figure 8b). Figures 8c–8e show the variation in dislocation microstructures in the larger grains. Many grains show high densities of tangled dislocations at grain-to-grain contacts, as well as linear arrays of closely spaced dislocations (Figures 8c, 8e, 8f). Microcracks are also observed to emanate from grain contacts (e.g., Figure 8c). The interior of some large grains exhibit dislocation densities similar to the starting material (Figure 8d).

3.3. Volumetric Strain

[15] Correlations among volumetric strain, differential stress, and microstructures indicate that mechanical behavior evolves owing to compaction. Volumetric strain curves are shown together with differential stress in Figures 9 and 10. All samples compact, while strain hardening, during the initial stage of the experiments. The compaction rate decreases as sample strength approaches a constant level. Deformation of sample OF-06 was terminated at this point (Figure 9c), revealing a developing fine-grained shear zone (Figure 6b). The volumetric strain behavior following localization depends on pressure and temperature. At the lowest P_C^{eff} and T, modest dilation was observed (Figure 9a). By contrast, at higher P_C^{eff} and T, the volumetric strain remained constant or exhibited modest compaction (Figure 10). The greatest compaction was observed at the highest pressure (Figure 9), and at constant P_C^{eff} the magnitude of compaction increased with increasing temperature (c.f., Figures 9c and 10b).

[16] The influence of axial strain rate on volumetric strain also changes with increasing P_C^{eff}. At the lowest pressures we observed a change from compaction to dilation with increasing loading rate (Figure 9a). By contrast, at higher pressure, compaction rates increase at higher loading rates, but the ratio of volumetric strain to axial strain is less than one. Therefore the slope of the volumetric strain curve decreases at higher loading rates (e.g., Figures 9c and 10b).

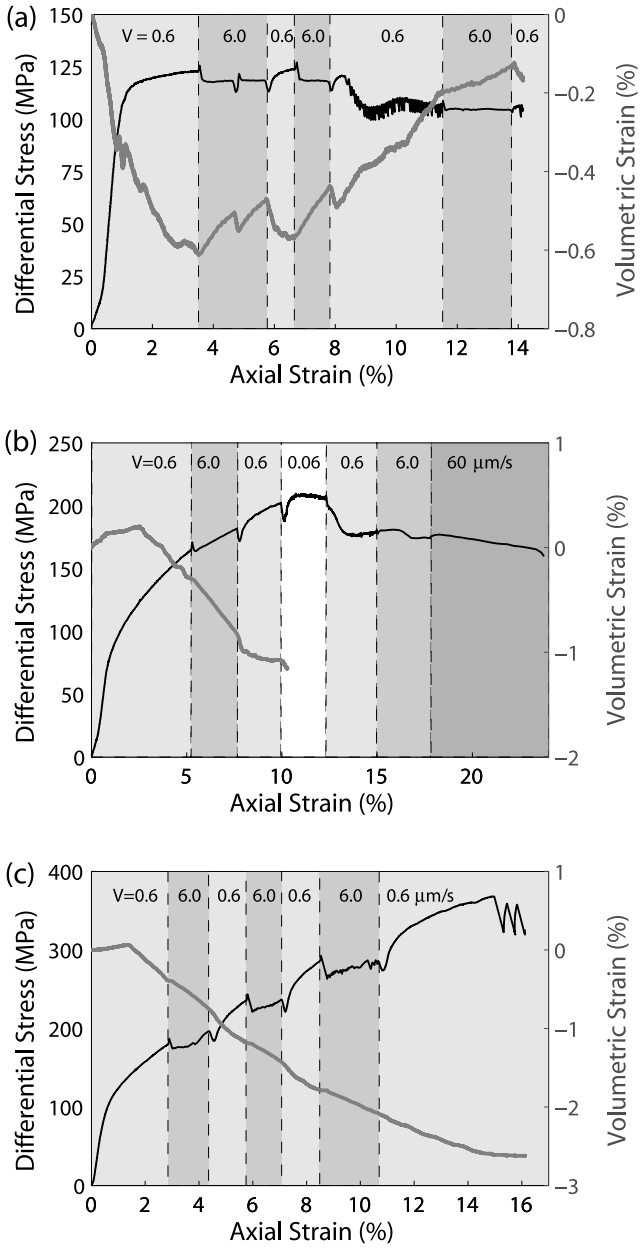

Figure 9. Differential stress (black curves) and volumetric strain (gray curves) for samples deformed at T = 800°C and P_C^{eff} = (a) 50 MPa (OF-05), (b) 100 MPa (OF-13), and (c) 200 MPa (OF-06). Changes in loading rate (indicated with background color) show velocity dependent effects of sample strength, volumetric strain, and frictional behavior. The perturbations in differential stress and compaction rate at 5.2% strain in Figure 9a resulted from rapidly imposed velocity steps from 6.0 to 0.6 and back to 6.0 μm/s. The volumetric strain record in Figure 9b is incomplete due to a pore pressure leak that initiated at 10.5% strain. Note that each panel is plotted at a different scale.

[17] For comparison with triaxial deformation experiments on granular aggregates, we show a plot of both maximum differential stress and yield stress as a function of effective mean stress in Figure 11, where effective mean stress is $1/3(\sigma_1 + 2P_C) - P_P$. Maximum strength shows a positive dependence on effective mean stress, consistent with coulomb failure. By contrast, yielding shows a negative pressure dependence, consistent with predictions for shear enhanced compaction [e.g., *Wong et al.*, 1997; *Xiao and Evans*, 2003; *Karner et al.*, 2005] and the observation that samples exhibit compaction during the initial stages of the experiments (Figures 9 and 10).

3.4. Velocity Dependence

[18] The velocity dependence of friction changes as a function of temperature, pressure, and strain. Order-of-magnitude steps in V were imposed to determine the sign of the friction rate parameter, $a - b$, in the rate and

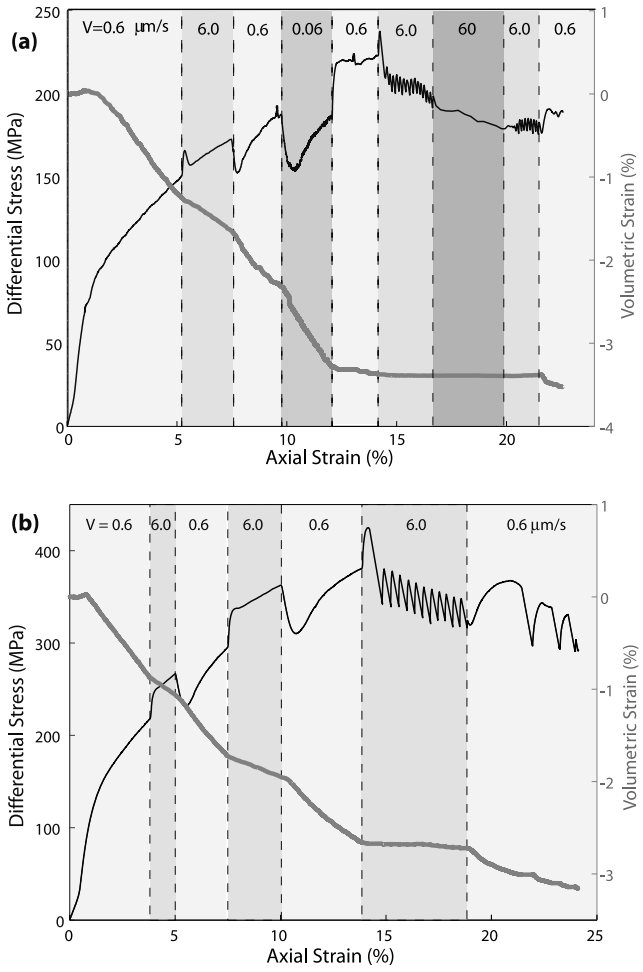

Figure 10. Differential stress (black) and volumetric strain (gray) data for experiments conducted at T = 1000°C and P_C^{eff} = (a) 100 MPa (OF-15) and (b) 200 MPa (OF-07). Changes in loading rate (indicated with background color) show velocity dependent effects of sample strength, volumetric strain, and frictional behavior. Note velocity-strengthening behavior is observed for the initial ~14% strain, followed by a change to velocity-weakening frictional conditions. Note that the panels are plotted at a different scale.

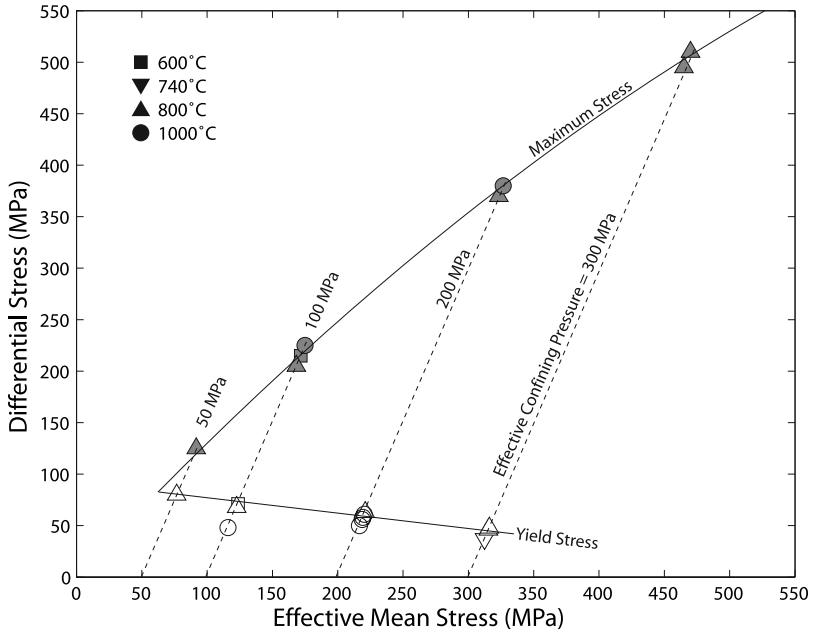

Figure 11. Differential stress verses effective mean stress, $1/3(\sigma_1 + 2P_C) - P_P$ at the onset on yielding (white symbols) and at maximum differential stress (gray symbols). Temperature is represented by the symbol shape. Data at each P_C^{eff} are indicated by the dashed lines. The solid curves connect (1) the maximum stress data with the best fit quadratic, $y = 1.36x - 6 \times 10^{-4}x^2$, and (2) the yield stress data with the best linear fit. Notice that the yield stress decreases with increasing effective mean stress consistent with the double surface yield cap model often used in soil mechanics and solid rock mechanics.

state dependent constitutive friction laws of the form [e.g., *Dieterich*, 1979; *Ruina*, 1983; *Marone*, 1998],

$$\mu = \mu_0 + a \ln\left(\frac{V}{V_0}\right) + b \ln\left(\frac{V_0\theta}{D_c}\right), \quad (3)$$

where μ_0 is the coefficient of friction during steady sliding at velocity V_0, θ is a state variable that evolves with either time or slip, a and b are empirical constants that quantify a direct effect and the state evolution following a change of velocity or normal stress, and D_c is the critical slip distance needed for μ to evolve to a new steady state following a change in loading conditions.

[19] The influence of temperature on the velocity dependence of friction is shown in Figure 4. All experiments conducted at or below 800°C exhibit velocity-weakening behavior, i.e. $a - b < 0$. The three velocity steps highlighted in the inset to Figure 4 were all conducted at $P_C^{eff} = 100$ MPa and axial strain between 7.5% and 10%. Velocity-weakening behavior is observed at 600°C and 800°C, with prominent stick-slip events evident at 600°C, and velocity-strengthening behavior is found at 1000°C. The velocity steps shown in Figure 4 are well suited for illustrating the transition from velocity weakening to velocity strengthening for a number of reasons: (1) they were all conducted at the same axial displacement and thus have similarly developed shear zones, (2) stable sliding was observed prior to the velocity steps, (3) the velocity steps are superimposed on only modest strain hardening curves, and (4) a relatively stable evolution to a new differential stress level was observed in all three cases. The 1000°C velocity-step continued at 0.6 μm/s to a displacement 0.14 mm further than shown in the inset (see the main plot of Figure 4 and Figure 10). Velocity strengthening was also observed in the subsequent two velocity steps during this experiment.

[20] The velocity steps shown in the inset to Figure 4 are presented as friction verses axial displacement in Figure 12a. On the basis of the relationships shown in Figure 5, we used a baseline friction value of 0.5 and calculated changes in friction with changes in velocity assuming $\mu = \tau/\sigma_n^{eff}$ and $\mu = 0.5$, i.e., a shear zone angle of 30 degrees. The data are compared to forward models calculated using the aging (Dieterich) evolution law in which θ evolves with both time and slip [*Dieterich*, 1979; *Ruina*, 1983],

$$\frac{d\theta}{dt} = 1 - \frac{V\theta}{D_c}, \quad (4)$$

and the known machine stiffness of 61 KN/mm. For each velocity step, the model provides a good fit to the magnitude of the direct effect and the evolution back to a steady-state level. The model also provides quantitative estimates for a, b, and D_C, which for the curves in Figure 12a are a = 0.010, 0.017, and 0.032, b = 0.013, 0.021, and 0.029, and D_C = 52, 100, and 185 μm at T = 600°C, 800°C, and 1000°C, respectively. No formal inversion was conducted; however, the range of parameter estimates that provide adequate fits to the velocity step data

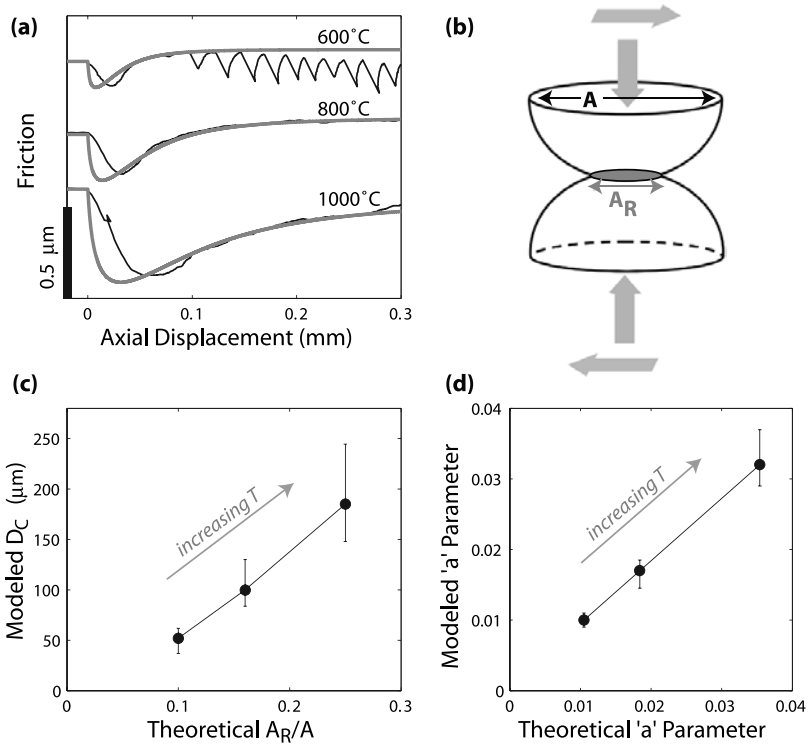

Figure 12. Observed, modeled, and theoretical friction parameters. (a) Detrended velocity steps (black), which are also shown in the inset of Figure 4, with forward model fits (gray). Data have been shifted to zero axial displacement and offset vertically from the initial friction levels: $\mu = 0.58$, 0.54, and 0.52 for $T = 600°C$, 800°C, and 1000°C respectively. (b) Cartoon of an asperity contact, where A is the nominal area of the sample and A_R is the real area of contact. Thick arrows denote the normal and shear forces loading the asperity. (c) A_R/A calculated from equation (5) versus the forward model fits of D_C from Figure 12a. (d) Friction parameter a calculated from equation (8) versus the forward model fits of a from Figure 12a. Thin bars in Figures 12c and 12d represent the range of parameter values that adequately fit the friction data.

are shown in Figures 12c and 12d. A significant mismatch, which can not be resolved with our model, exists between the measured and modeled rate of decrease immediately following the step change in V. Such an effect is common when modeling velocity decreases in friction experiments (C. Marone, personal communication, 2005). The model results indicate that the friction parameters all increase in magnitude at higher temperatures.

[21] The friction rate parameter $a - b$ also depends on effective confining pressure. The clearest example of velocity-strengthening behavior occurred at 1000°C and P_C^{eff} = 200 MPa at low axial strain (Figure 10). Velocity steps from 0.6 to 6.0 μm/s conducted at 1000°C resulted in a 15% strength increase at P_C^{eff} = 200 MPa, compared to only a 5% increase at P_C^{eff} = 100 MPa (Figure 10). These data indicate that $a - b$ at P_C^{eff} = 200 MPa is four times greater than that at P_C^{eff} = 100 MPa. The influence of effective confining pressure on $a - b$ is not as great at lower temperatures.

[22] The degree of localization significantly affected the frictional behavior of our samples. At 1000°C, a change in velocity dependence occurred at about 14% axial strain (Figure 10). For both samples, the change in frictional behavior correlated with a loading rate increase from 0.6 to 6.0 μm/s. Shear displacement measured from the enstatite strain marker in sample OF-15 shows that the transition occurred just before deformation localized onto discrete sliding surfaces (Figure 4).

4. Discussion

[23] A combination of mechanical and microstructural data indicates that deformation is accommodated by macroscopically brittle processes during our high temperature triaxial experiments on initially homogeneous olivine aggregates. In addition, the response to changes in loading rate is well described by rate and state friction laws, even during the initial stages of experiments (i.e., prior to the formation of discrete shear surfaces such as those illustrated in Figure 7). These observations indicate that the grain-scale processes that control the rheological behavior of our samples are the same as those in standard frictional sliding experiments [e.g., *Karner et al.*, 2005]. Specifically, in both types of experiments deformation is accommodated by a combination of granular flow and cataclasis. Furthermore, microstructural evidence for dislocation activity indicates that intracrystalline plasticity plays an important role in the

deformation process. Our observations also suggest that strain localization initiated early in the experiments, while samples were still compacting (Figures 3, 4, and 9). The process responsible for localization may be similar to that modeled by *Rudnicki and Rice* [1975]. While total axial displacement is limited, our experiments clearly provide a good way to evaluate frictional behavior at temperatures relevant to conditions in the Earth. We address the parameters controlling frictional behavior through an analysis of the physical basis for rate and state friction and discuss implications of our results for the base of oceanic seismogenic zones.

4.1. Rate-State Analysis

[24] The effects of pressure, temperature, and loading rate on the frictional behavior of our samples are systematic and are well described by the classic models of friction [e.g., *Bowden and Tabor*, 1950; *Greenwood and Williamson*, 1966; *Dieterich and Kilgore*, 1996]. In particular, our results are consistent with *Bowden and Tabor*'s [1950, 1966] adhesion theory, which describes friction as the response to elastic and inelastic deformation of strong asperities. Bowden and Tabor's hypothesis predicts a linear pressure dependence of the bulk sample strength that is independent of temperature. At the asperity scale, however, deformation can be described by temperature and strain rate dependent plasticity laws.

[25] Several observations indicate that plastic yielding occurs at asperities in our samples, including (1) high dislocation densities near grain contacts, (2) a decrease in yield stress with increasing temperature at constant pressure, and (3) greater compaction with increasing temperature at constant pressure. We conclude that higher temperatures enhance compaction by promoting plastic flow at grain-to-grain contacts, i.e. asperities (e.g., Figure 8). In the following discussion, we explore how these observations, combined with an analysis of temperature-dependent contact properties, can be used to explain the velocity dependence of friction observed in our data [e.g., *Chester*, 1994, 1995; *Rice et al.*, 2001; *Nakatani*, 2001]. Our data are particularly well suited for this analysis because the temperature and stress dependence of olivine plasticity are constrained for the conditions of our experiments.

[26] Motivated by the microstructural observations, we hypothesize that deformation of the asperities occurs according to flow laws determined from indentation creep tests on olivine single crystals [*Goetze*, 1978; *Evans and Goetze*, 1979]. At the temperatures and axial strain rates used in our experiments, single crystal strengths are a factor of two to four times greater than frictional strengths at the same conditions. Plastic flow at the asperities is promoted by stress concentrations at grain-to-grain contacts, which result in a significant difference between the "real" load-bearing area of contact, A_R, and the nominal area, A, of our samples. For single crystals the ratio $A_R/A = 1$, while for our samples, which we model as a granular media, $A_R/A < 1$. The cartoon in Figure 12a illustrates this difference schematically for the simple case of two grains. Our samples are composed of many grains, and thus A_R is the sum of a large number of microcontacts [e.g., *Baumberger et al.*, 2001].

[27] We take a similar approach to *Tullis and Weeks* [1987] and *Reinen et al.* [1994] and calculate A_R/A by assuming that the pressure-dependent sample strengths follow the relation,

$$\frac{A_R}{A} = \frac{\sigma_1 - \sigma_3}{\sigma_A}, \tag{5}$$

where the yield stress at the asperity, σ_A, is the single crystal strength. We calculate σ_A using the low-temperature plasticity flow law of [*Goetze*, 1978]:

$$\sigma_A = \sigma_P \left[1 - \left(\frac{-RT}{H} \ln \frac{\dot{\epsilon}}{B} \right)^{1/q} \right], \tag{6}$$

where the Peierl's stress σ_P = 8500 MPa, the gas constant R = 8.314 J/mol/K, the activation enthalpy $H = 5.4 \times 10^5$ J/mol, the empirical constant $B = 5.7 \times 10^{11}$ s^{-1}, and the exponent q = 2. Substitution of equation (6) into equation (5) predicts that A_R/A increases with increasing temperature owing to a decrease in σ_A, and, based on our observations, no change in $\sigma_1 - \sigma_3$. For the three P_C^{eff} = 100 MPa experiments shown in Figure 4, we calculate A_R/A = 0.10, 0.16, and 0.25 at 600°C, 800°C, and 1000°C, respectively.

[28] The predicted temperature dependence of A_R/A indicates that the asperity contact size also increases with increasing temperature. From the rate and state description of friction, D_C is the sliding distance necessary to renew a contact population following a change in loading conditions. From the aging law (equation (4)), $D_C/V = \theta$ at steady state, where θ is an average contact lifetime and D_C is an average contact size. As shown in Figure 12c, the predicted increase in A_R/A is proportional to our measured increase in D_C. Thus consistent with adhesion theory, the size and strength of asperities apparently trade off in such a way as to maintain an overall sample strength that increases linearly with pressure, independent of temperature.

[29] Constraints on the temperature and stress dependence of olivine plasticity also allow us to explore a physical basis for the "direct effect" and calculate a theoretical value for the rate parameter, a. We follow previous experimental and theoretical studies [see *Chester*, 1995; *Rice et al.*, 2001, and references therein] and assume that the second term in equation (3) arises from the Arrhenius process that controls creep at the asperity. In this case, the slip rate can be written as

$$V = V_0 \exp\left(\frac{-E}{k_B T} \right), \tag{7}$$

where $E = E' - \tau_A \Omega$ is the activation energy, Ω is the activation volume, and $\tau_A = \mu\sigma_A$ is the average shear stress at asperity contacts. Substituting equation (7) into equation (3) and rearranging, leads to a theoretical formulation of the parameter a,

$$a = \frac{k_B T}{\sigma_A \Omega}, \tag{8}$$

where $k_B = 1.38 \times 10^{-23}$ m^{2}kg/s^{2}K is Boltzman's constant. Figure 12d shows that theory and observations match well

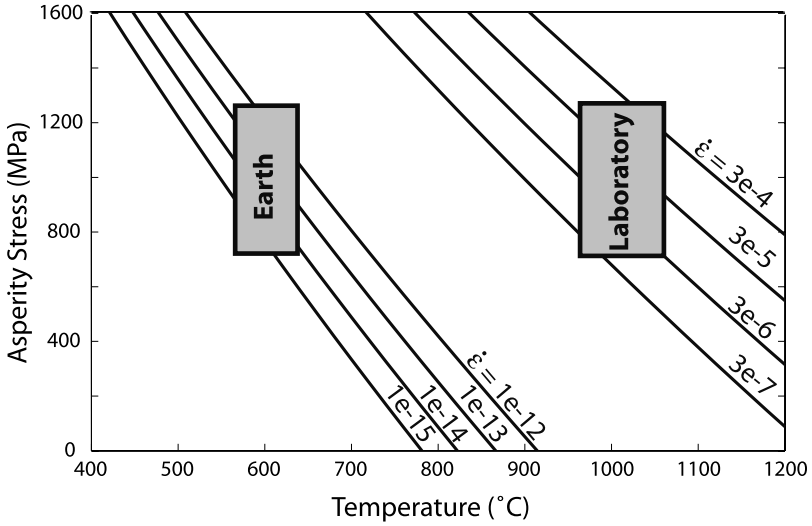

Figure 13. Scaling between laboratory experiments and natural conditions assuming the stress at the asperity is a material property. Curves calculated with equation (6) are shown for tectonic strain rates and for the strain rates used in laboratory experiments. Boxes indicate observed (laboratory) and calculated (Earth) conditions at which a transition between velocity-weakening and velocity-strengthening behavior occurs.

when $\Omega = 5 \times 10^{-28}$ m^3 (which is approximately twice the molecular volume for olivine). Values of Ω on this order also match room temperature data for quartzite, where σ_A calculated from the theoretical strength, i.e., 1/10 shear modulus [*Rice et al.*, 2001], and high temperature friction experiments on plagioclase [*Nakatani*, 2001].

[30] At face value, the agreement between the Arrhenius relationship and the experimental data is encouraging. However, we caution against placing too much significance on the calculated Ω values. First, Ω should not be confused with the "activation volume" that describes the role of pressure on kinetic processes. Rather, physical models for thermally activated dislocation glide suggest that Ω is better referred to as the product $\vec{b}A^*$ [*Hirth and Lothe*, 1982], where $\vec{b}$ is the Burgers vector and A^* is an activation area; $A^* = la^*$, where l is the length of the pinned dislocation segment and A^* is the distance the dislocation segment moves to overcome the energy barrier for glide. Because $l \approx 100\vec{b}$, and $A^* \approx \vec{b}$ [e.g., *Hirth and Lothe*, 1982], the calculated values of Ω on the order of the molecular volume (i.e., $\Omega \approx \vec{b}^3$) may be an artifact of not accounting for additional stress dependent terms in equation (7) [e.g., see *Mitchell and Heuer*, 2004]. Indeed, the exponent $q = 2$ in equation (6) suggests additional stress-dependence in the low temperature plasticity flow law determined for olivine.

[31] The olivine flow laws can also be used to explore the physical basis for the "evolution effect" and calculate a theoretical value for b. The third term in equation (3) describes an aging (or evolution) effect that is, following adhesion theory, directly related to the strain-rate sensitivity of crystal plasticity at contact asperities. As described by *Baumberger et al.* [2001; see also *Paterson and Wong*, 2005], $b \approx \mu_0/n$, where n is the power law exponent in $\dot{\epsilon} \propto \sigma^n$. We calculated the effective stress exponent at $\dot{\epsilon} = 1 \times 10^{-5}$ s^{-1} using equation (6) and found $n = 30$, 19, and 12 at 600°C, 800°C, and 1000°C, respectively. Taking these n values, and assuming μ_0 equal to the coefficient of friction prior to the velocity step, we calculate $b = 0.019$ (0.013), 0.028 (0.021), and 0.043 (0.029), respectively; with our observed values given in parenthesis. We thus see a positive correlation between our measured b values and the theoretically derived estimates, consistent with the hypothesized relationship between the evolution effect and the strain-rate sensitivity of asperity rheology. However, the calculated values of b are approximately 50% greater than the observed values. This discrepancy may arise owing to uncertainties in the strain rate dependence of deformation at these conditions.

4.2. Implications

[32] Our experimental data demonstrate that velocity-weakening behavior is observed to high temperatures under dry conditions in olivine aggregates. At face value, this result appears more consistent with geophysical observations than *Stesky et al.*'s [1974] findings, which showed velocity strengthening behavior at temperatures as low as 200°C. On the basis of the general agreement between our data and the application of temperature-dependent crystal plasticity to rate and state friction, we extrapolate our data to constrain the conditions where a velocity-weakening/strengthening transition occurs in the Earth. For this analysis, we assume that the transition between velocity weakening and strengthening occurs when the deformation conditions at contact asperities are the same in the Earth and our laboratory experiments. Specifically, we analyze the tradeoff between temperature and strain rate to determine the conditions where the stress at the asperity is predicted to be the same in the Earth and the lab. In our experiments, where the transition in frictional behavior is observed at about 1000°C, the value of σ_A is in the range of 800–1200 MPa. Using equation (6), we extrapolate the experimental results to conditions appropriate for the oceanic mantle (Figure 13). For tectonic strain rates 10^{-15} s$^{-1} \leq \dot{\epsilon} \leq 10^{-12}$ s^{-1}, we predict that the base of

the velocity-weakening layer should be at a temperature between 550 and 650°C.

[33] Deformation in our experiments spans the transition from unstable to stable frictional sliding, but we do not observe fully ductile behavior. Triaxial deformation experiments conducted on olivine aggregates indicate that power-law creep initiates at temperatures of around 1100–1200°C [*Beeman and Kohlstedt*, 1993; *Zimmerman and Kohlstedt*, 2004], indicating that our experimental conditions are near the brittle/plastic transition. In addition, increasing confining pressure will promote a transition to ductile flow. Our results also suggest that with additional experimental data a more sophisticated analysis could account for the role of porosity evolution on the stability of frictional sliding at high temperature.

[34] Observations from both seismic and aseismic deformation are consistent with our conclusion that the 600°C isotherm is the approximate base of the seismogenic zone in oceanic lithosphere. Earthquake focal depths, calculated from ocean bottom seismicity [*Wilcock et al.*, 1990] and teleseismic studies using waveform modeling and slip inversions [*Abercrombie and Ekström*, 2001, 2003], correlate with temperatures of $T \leq 600$°C. Furthermore, mylonites collected from the Shaka fracture zone on the South West Indian Ridge provide additional evidence for the location of the boundary between seismic and aseismic deformation. The microstructures preserved in the mylonites indicate that they formed during localized viscous deformation at temperatures in the range of 600–800°C [*Warren and Hirth*, 2006]. Thus our experiments, seismological observations, and microstructures from oceanic dredge samples all point to approximately 600°C as the bounding isotherm for seismic activity in the oceanic lithosphere.

5. Conclusions

[35] During triaxial compression tests on olivine powders, localized fine-grained shear zones developed. Deformation resulted in systematic differential stress and volumetric strain curves that varied with pressure, temperature, axial strain, and loading rate. Our results span the frictional regimes from the velocity-weakening to the velocity-strengthening, with a transition at approximately 1000°C at our laboratory strain rates. Microstructural observations indicate that crystal plasticity is promoted by stress concentrations at grain contacts. At higher temperatures we observed evidence for a decrease in asperity strength, an increase in asperity contact area, and an increase in each of the rate-state friction parameters a, b, and D_C. Our data support the physical basis for rate and state friction laid out by previous workers, in which stress concentrations and the resulting deformation at contact asperities control frictional behavior. Using flow laws determined from deformation tests of olivine single crystals, we extrapolate our results to conditions appropriate for the Earth. This analysis leads to the prediction that the 600°C isotherm is the approximate limit of the seismogenic zone in the oceanic lithosphere, consistent with geophysical observations.

[36] **Acknowledgments.** We thank Xiaohui Xiao for all of his help and experimental expertise, Chris Marone and Laurent Montesi for insightful discussions and Chris for providing his forward modeling code, Glenn Gaetaeni for generously allowing us to use his laboratory facilities, and Steve Karner for his thoughtful review. This research was supported by the Deep Ocean Exploration Institute at WHOI and NSF grants to Greg Hirth and Brian Evans.

References

Abercrombie, R., and G. Ekström (2001), Earthquake slip on oceanic transform faults, *Nature*, *410*, 74–77.

Abercrombie, R., and G. Ekström (2003), A reassessment of the rupture characteristics of oceanic transform earthquakes, *J. Geophys. Res.*, *108*(B5), 2225, doi:10.1029/2001JB000814.

Baumberger, T., P. Berthoud, and C. Caroli (2001), Physical analysis of the state- and rate- dependent friction law. ii. Dynamic friction, *Phys. Rev. B*, *60*(6), 3928–3939.

Beeler, N., T. Tullis, M. Blanpied, and J. Weeks (1996), Frictional behavior of large displacement experimental faults, *J. Geophys. Res.*, *101*, 8697–8715.

Beeman, M. L., and D. L. Kohlstedt (1993), Deformation of fine-grained aggregates of olivine plus melt at high temperatures and pressures, *J. Geophys. Res.*, *98*, 6443–6452.

Bergman, E. A., and S. C. Solomon (1988), Transform fault earthquakes in the North Atlantic: Source mechanisms and depth of faulting, *J. Geophys. Res.*, *93*, 9027–9057.

Bowden, F., and D. Tabor (1950), *The Friction and Lubrication of Solids*, p. 374, Oxford Univ. Press, New York.

Bowden, F., and D. Tabor (1966), Friction, lubrication, and wear: A survey of work done during the last decade, *Brit. J. Appl. Phys.*, *17*, 1521–1544.

Brace, W. F., B. W. Paulding Jr., and C. Scholz (1966), Dilatancy in the fracture of crystalline rocks, *J. Geophys. Res.*, *71*, 3939–3953.

Byerlee, J. (1978), Friction of rocks, *Pure Appl. Geophys.*, *116*, 615–626.

Chester, F. M. (1994), Effects of temperature on friction: Constitutive equations and experiments with quartz gouge, *J. Geophys. Res.*, *99*, 7247–7261.

Chester, F. M. (1995), A rheologic model for wet crust applied to strike-slip faults, *J. Geophys. Res.*, *100*, 13,033–13,044.

Dieterich, J. H. (1979), Modeling of rock friction: 1. Experimental results and constitutive equations, *J. Geophys. Res.*, *84*, 2161–2168.

Dieterich, J. H., and B. Kilgore (1996), Implications of fault constitutive properties for earthquake prediction, *Proc. Natl. Acad. Sci. USA*, *93*, 3787–3794.

Engeln, J. F., D. A. Weins, and S. Stein (1986), Mechanisms and depths of Atlantic transform earthquakes, *J. Geophys. Res.*, *91*, 548–577.

Escartin, J., G. Hirth, and B. Evans (1997), Non-dilatant brittle deformation of serpentinites: Implications for Mohr-Coulomb theory and the strength of faults, *J. Geophys. Res.*, *102*, 2897–2913.

Evans, B., and C. Goetze (1979), The temperature variation of hardness of olivine and its implications for polycrystalline yield stress, *J. Geophys. Res.*, *84*, 5505–5524.

Evans, B., J. T. Frederich, and T.-F. Wong (1990), The brittle-ductile transition in rocks: Recent experimental and theoretical progress, in *The Brittle-Ductile Transitions in Rocks: The Heard Volume*, *Geophys. Monogr. Ser.*, vol. 56, edited by A. G. Duba et al., pp. 1–20, AGU, Washington, D. C.

Goetze, C. (1978), Mechanisms of creep in olivine, *Phil. Trans. R. Soc. London, Ser. A*, *288*, 99–119.

Greenwood, J., and J. Williamson (1966), Contact of nominally flat surfaces, *Proc. R. Soc. London, Ser. A*, *295*, 300–319.

Hirth, J. P., and J. Lothe (1982), *Theory of Dislocations*, 2nd ed., John Wiley, Hoboken, N. J.

Karner, S. L., F. M. Chester, and J. S. Chester (2005), Towards a general state-variable constitutive relation to describe granular deformation, *Earth Planet. Sci. Lett.*, *237*, 940–950.

Kohlstedt, D., C. Goetze, W. Durham, and J. V. Sande (1976), New technique for decorating dislocations in olivine, *Science*, *191*(4231), 1045–1046.

Marone, C. (1998), Laboratory derived friction laws and their application to seismic faulting, *Annu. Rev. Earth Planet. Sci.*, *26*, 643–696.

McKenzie, D., J. Jackson, and K. Priestley (2005), Thermal structure of oceanic and continental lithosphere, *Earth Planet. Sci. Lett.*, *233*, 337–349.

Mitchell, T., and A. Heuer (2004), Dislocations and mechanical properties of ceramics, in *Dislocations in Solids*, vol. 12, edited by F. Nabarro and J. Hirth, pp. 339–402, Elsevier, New York.

Nakatani, M. (2001), Conceptual and physical clarification of rate and state friction: Frictional sliding as a thermally activated rheology, *J. Geophys. Res.*, *106*, 13,347–13,380.

Paterson, M. S. (1978), *Experimental Rock Deformation—The Brittle Field*, Springer, New York.

Paterson, M. S. (1990), Rock deformation experimentation, in *The Brittle-Ductile Transitions in Rocks: The Heard Volume*, *Geophys. Monogr. Ser.*, vol. 56, edited by A. G. Duba et al., pp. 187–194, AGU, Washington, D. C.

Paterson, M. S., and T. Wong (2005), *Experimental Rock Deformation—The Brittle Field*, Springer, New York.

Reinen, L. A., J. D. Weeks, and T. E. Tullis (1994), The frictional behavior of lizardite and antigorite serpentinites: Experiments, constitutive models, and implications for natural faults, *Pure Appl. Geophys.*, *143*, 317–385.

Rice, J. R., N. Lapusta, and K. Janjith (2001), Rate and state dependent friction and the stability of sliding between elastically deformable solids, *J. Mech. Phys. Solids*, *49*, 1865–1898.

Rudnicki, J., and J. Rice (1975), Conditions for the localization of deformation in pressure-sensitive dilatant materials, *J. Mech. Phys. Solids*, *23*, 371–394.

Ruina, A. L. (1983), Slip instability and state variable friction laws, *J. Geophys. Res.*, *88*, 10,359–10,370.

Scholz, C. H. (2002), *The Mechanics of Earthquakes and Faulting*, 2nd ed., Cambridge Univ. Press, New York.

Shimada, M., A. Cho, and H. Yukatake (1983), Fracture strength of dry silicate rocks at high confining pressures and activity of acoustic emission, *Tectonophysics*, *96*, 159–172.

Stein, S., and A. Pelayo (1991), Seismological constraints on stress in the oceanic lithosphere, *Phil. Trans. R. Soc. London, Ser. A*, *337*, 53–72.

Stesky, R. M. (1978a), Rock friction-effect of confining pressure, temperature, and pore pressure, *Pure Appl. Geophys.*, *116*(4-5), 690–704.

Stesky, R. M. (1978b), Mechanisms of high temperature frictional sliding in Westerly granite, *Can. J. Earth Sci.*, *15*(3), 361–375.

Stesky, R. M., W. F. Brace, D. K. Riley, and P.-Y. F. Robin (1974), Friction in faulted rock at high temperature and pressure, *Tectonophysics*, *23*(1-2), 177–203.

Tullis, T. E., and J. D. Weeks (1987), Micromechanics of frictional resistance of calcite, *Eos Trans. AGU*, *68*, 405.

Warren, J., and G. Hirth (2006), Grain size sensitive deformation mechanisms in naturally deformed peridotites, *Earth Planet. Sci. Lett.*, *248*, 423–435.

Wiens, D. A., and S. Stein (1983), Age dependence of oceanic intraplate seismicity and implications for lithospheric evolution, *J. Geophys. Res.*, *88*, 6455–6468.

Wilcock, W., G. Purdy, and S. Solomon (1990), Microearthquake evidence for extension across the Kane Transform Fault, *J. Geophys. Res.*, *95*, 15,439–15,462.

Wong, T., C. David, and W. Zhu (1997), The transition from brittle faulting to cataclastic flow in porous sandstones: Mechanical deformation, *J. Geophys. Res.*, *102*, 3009–3025.

Xiao, X., and B. Evans (2003), Shear-enhanced compaction during nonlinear viscous creep of porous calcite-quartz aggregates, *Earth Planet. Sci. Lett.*, *216*, 725–740.

Zimmerman, M. E., and D. L. Kohlstedt (2004), Rheological properties of partially molten lherzolite, *J. Petrol.*, *45*(2), 275–298.

M. S. Boettcher, United States Geological Survey, Mail Stop 977, 345 Middlefield Road, Menlo Park, CA 94025, USA. (mboettcher@usgs.gov)

B. Evans, Department of Earth, Atmospheric, and Planetary Sciences, Massachusetts Institute of Technology, Cambridge, MA 02139, USA. (brievans@mit.edu)

G. Hirth, Department of Marine Geology and Geophysics, Woods Hole Oceanographic Institution, Woods Hole, MA 02543, USA. (ghirth@whoi.edu)